

Sand ripples and dunes

FRANÇOIS CHARRU

*Institut de Mécanique des Fluides de Toulouse – CNRS-INP-UPS - Université
de Toulouse,*
2 allée C. Soula, 31400 Toulouse, France. E-mail: francois.charru@imft.fr

BRUNO ANDREOTTI

Laboratoire de Physique et Mécanique des Milieux Hétérogènes,
(PMMH UMR 7636 ESPCI - CNRS - Univ. Paris Diderot - Univ. P. M. Curie.)
10 rue Vauquelin, 75005 Paris, France. E-mail: andreotti@pmmh.espci.fr

PHILIPPE CLAUDIN

Laboratoire de Physique et Mécanique des Milieux Hétérogènes,
(PMMH UMR 7636 ESPCI - CNRS - Univ. Paris Diderot - Univ. P. M. Curie.)
10 rue Vauquelin, 75005 Paris, France. E-mail: claudin@pmmh.espci.fr

Key Words bedforms, sediment transport, relaxation phenomena, instability,
turbulent flow, laminar flow

Abstract An erodible bed sheared by a fluid flow, gas or liquid, is generally unstable, and bedforms grow. The following questions are discussed, in the light of the recent literature:

What are the relevant dynamical mechanisms controlling the emergence of bedforms? Do they form by linear instability or nonlinear processes like pattern-coarsening? What determines their time and length scales, so different in air and water? What are the similarities and differences between aeolian and subaqueous patterns? What is the influence of the mode of transport: bedload, saltation or suspension? Can bedforms emerge under any hydrodynamical regime, laminar and turbulent? Guided by these questions, a unified description of bedform growth and saturation is proposed, with emphasis on the hydrodynamical regime in the inner layer and the relaxation phenomena associated with particle transport.

CONTENTS

Introduction	3
Hydrodynamics over a wavy bottom in the unbounded limit	4
<i>Flow over a flat bottom</i>	4
<i>Linear response of the flow to a wavy wall</i>	6
<i>Beyond the linear response</i>	11
The scales of particle transport	13
<i>What is the hydrodynamic parameter controlling transport?</i>	13
<i>Linear response of the saturated flux</i>	16
<i>What are the dynamical mechanisms controlling sediment transport?</i>	17
Stability analysis of a flat erodible bed	20
<i>Dispersion relation</i>	20
<i>Linear wavelength selection</i>	21
<i>Nonlinear coarsening</i>	26
Finite size effects	26
<i>Hydrodynamics</i>	27
<i>Linear instability and pattern formation</i>	28
Conclusion	29

Summary Points 29

Future issues 31

Side bar: oscillating ripples 31

Key Terms and Definitions 32

1 Introduction

Sand or granular patterns may emerge from an erodible bed sheared by a fluid flow in a wide variety of environments: in water channels, rivers and coastal areas (Best 2005), in deserts on Earth (Bagnold 1941, Pye & Tsoar 1990) and under methane or CO_2 atmospheres on other planets (Bourke et al. 2010), in hydraulic engineering and industrial pipe flows (Schaffinger et al. 1995, Stevenson et al. 2001). Their size can range from the centimeter scale for subaqueous ripples to one hectometer for large river megadunes, from one decameter for the smallest aeolian dunes to one kilometer for the largest ones. Mature, finite-height bedforms are typically asymmetric, with an avalanche slip face on their lee side. More generally, bedforms exhibit different shapes depending on the symmetries of the fluid forcing, or the boundary conditions (see definitions in the margin) (Andreotti et al. 2009, Fryberger & Dean 1979). The dynamics of these patterns results from the interaction between the fluid flow and the bed topography through particle transport. For unidirectional flow (Figure 1), the fluid accelerates on the windward slope and decelerates on the lee side. Grains are therefore eroded upstream of the crest and deposited downstream. The resulting migrating velocity c is inversely proportional to the dune height H (Figure 1), a simple result of great importance which arises from mass conservation (Bagnold 1941).

The wide occurrence of sand patterns has stimulated a huge number of studies aiming at their understanding. Since the pioneering book of Bagnold (1941), significant progresses have been achieved which were reviewed, notably, by Engelund & Fredsøe (1982) for ripples and dunes, Blondeaux (2001) for coastal forms, and Seminara (2011) for fluvial sedimentary patterns. Some important issues, still debated, are the following. What are the relevant dynamical mechanisms controlling the emergence of bedforms? Do they form by linear instability or non-linear processes like pattern-coarsening? What determines their time and length scales, so different in air and water? What are the similarities and differences between aeolian and subaqueous patterns? (Figure 1) What is the influence of the mode of transport: bedload, saltation or suspension? Can bedforms emerge under any hydrodynamical regime, laminar and turbulent? The aim of the present review is to propose, from the recent literature, a unified description of bedform growth and a hierarchy of the relevant parameters and corresponding regimes. For this purpose, we focus on the canonical situation of transverse bedforms under an unbounded, steady, unidirectional flow. The paper is organized as follows. In Section 2, the hydrodynamics above an undulated fixed bottom is reviewed. In Section 3, we discuss the dynamics of sediment transport. Section 4 is devoted to the linear stability analysis of a flat bed, and some nonlinear developments. Finite size effects are finally discussed in Section 5.

2 Hydrodynamics over a wavy bottom in the unbounded limit

2.1 Flow over a flat bottom

Consider the flow of a fluid with kinematic viscosity ν and density ρ_f , exerting on a flat bottom a shear stress $\tau_0 = \rho_f u_*^2$ where u_* is the friction velocity. x ,

y and z denote the streamwise and spanwise directions and the normal to the bottom, respectively. The bottom is composed of grains of characteristic diameter d , located at $z = 0$ (for a precise definition of this location, see e.g. Raupach et al. (1991)). Far enough from the bed, the flow is generally turbulent with logarithmic velocity profile

$$U(z) = \frac{u_*}{\kappa} \ln \left(\frac{z}{z_0} \right), \quad (1)$$

where $\kappa \approx 0.4$ is the von Kármán constant. This ‘law of the wall’ (Raupach et al. 1991) involves a length z_0 , called the hydrodynamical roughness, which is picked up by the matching with a surface layer. For d small enough, the surface layer corresponds to the viscous sublayer, with thickness of about 6 times the viscous length $\delta_\nu = \nu/u_*$ and linear velocity profile

$$U(z) = (u_*/\delta_\nu)z. \quad (2)$$

The flow is said dynamically smooth and the hydrodynamical roughness is given by $z_0 \approx 0.11 \delta_\nu$. A good estimate of the full velocity profile can be obtained from the momentum equation $u_*^2 = (\nu + \ell^2 U'(z))U'(z)$ with an exponential damping of the Prandtl mixing length as the bed is approached,

$$\ell = \kappa z (1 - \exp(-z/\alpha\delta_\nu)) \quad (3)$$

where $\alpha \approx 25$ is the van Driest number (Pope 2000). For d larger than, say, one tens of δ_ν , the viscous sublayer is no longer relevant and the flow is said hydrodynamically rough. Measurements then give, for fixed grains, $z_0 \approx 0.03 - 0.1 d$ (Andreotti 2004, Bagnold 1941, Kamphuis 1974). A usual yet phenomenological description introduces the mixing length (Ayotte et al. 1994, Colombini 2004, Fourrière et al. 2010, Richards 1980)

$$\ell = \kappa(z + z_0). \quad (4)$$

The existence of a layer of moving grains at the bed surface may increase the roughness z_0 , see Section 3.

2.2 Linear response of the flow to a wavy wall

2.2.1 STRUCTURE OF THE FLOW DISTURBANCE AND BOTTOM SHEAR STRESS.

Now consider a disturbed bottom, in the simplest situation of small amplitude two-dimensional waves, $\zeta = \zeta_0 \cos kx$. Typical values of the parameters are given in Table 1. For small wave slope, typically $k\zeta_0 < 0.1$ ($2\zeta_0/\lambda < 0.03$), the flow disturbance is sinusoidal and proportional to $k\zeta_0$, i.e. the response is linear. The measurements displayed in Figure 2 show such a linear response of the shear stress τ_b , and the presence of higher harmonics for larger slope. Note, in particular, the phase advance with respect to the bottom. The linear stability problem amounts to the determination, for small slope, of

$$\tau_b = \frac{1}{2} \left(\hat{\tau} e^{ikx} + \hat{\tau}^* e^{-ikx} \right), \quad \hat{\tau} = \tau_0 (\mathcal{A} + i\mathcal{B}) k\zeta_0, \quad (5)$$

where \mathcal{A} and \mathcal{B} are the components in-phase and in-quadrature with the bottom, respectively. This subsection focuses on the unbounded limit, $kD \gg 1$, where the vertical extent D of the flow is larger than the penetration depth $\approx 2\pi/k$ of the flow disturbance, so that \mathcal{A} and \mathcal{B} depend on the single parameter kz_0 .

Figure 3 shows measurements as well as theoretical predictions of $\mathcal{A}(kz_0)$ and $\mathcal{B}(kz_0)$. The reference curve, the black solid line, is based on the Reynolds-averaged Navier-Stokes (RANS) equations and the mixing length (3). For given base flow, four hydrodynamical regimes can be identified, controlled by kz_0 , which are detailed below.

2.2.2 VISCOUS AND INERTIAL LAMINAR REGIMES. At large wavenumbers,

the flow disturbance is confined within the viscous sublayer where the veloc-

ity profile (2) is linear. The problem can therefore be solved by neglecting the turbulent fluctuations (Benjamin 1959, Charru & Hinch 2000, Valance & Langlois 2005). Figure 3a-b shows that the corresponding \mathcal{A} and \mathcal{B} (yellow curve) matches, in effect, for $k\delta_\nu \gtrsim 10^{-2}$, the calculation including the Reynolds stresses (red curve). The flow disturbance has a two-layered structure sketched in Figure 3c: an outer layer (green) dominated by inertia and an inner layer (orange) dominated by viscosity, where the flow is driven by the pressure gradient inherited from the outer layer. The thickness δ_i of the inner layer can be defined from the balance of longitudinal advection ($\sim k(u_*^2/\nu)\delta_i$) and transverse viscous diffusion ($\sim \nu/\delta_i^2$), giving

$$\delta_i \sim (\nu^2/k u_*^2)^{1/3} = (\delta_\nu^2/k)^{1/3}. \quad (6)$$

δ_i also represents the penetration depth of vorticity disturbances, so that the flow disturbance in the outer layer is potential. Asymptotic expressions of \mathcal{A} and \mathcal{B} have been derived in the viscous and inertial regimes (orange and green dashed lines) by Benjamin (1959) and Charru & Hinch (2000):

$$\mathcal{A} + i\mathcal{B} = 2 + i\frac{1}{2}(k\delta_i)^{-3} = 2 + i\frac{1}{2}(k\delta_\nu)^{-2} \quad (k\delta_i \gg 1) \quad (7)$$

$$\mathcal{A} + i\mathcal{B} = \gamma_L (k\delta_i)^{-1} e^{i\pi/6} = \gamma_L (k\delta_\nu)^{-2/3} e^{i\pi/6} \quad (k\delta_i \ll 1) \quad (8)$$

where $\gamma_L \approx 1.06$. Figure 3 shows that these expressions are close to the exact calculation (yellow curve).

2.2.3 TURBULENT REGIME. For small wavenumber, the flow disturbance extends far beyond the surface layer so that Reynolds stresses cannot be neglected. Figure 3 shows that \mathcal{A} and \mathcal{B} depend slowly on kz_0 , logarithmically, as expected. The asymptotic analysis has first been tackled by Jackson & Hunt (1975) and then improved in several ways, notably by Sykes (1980), see the review by Belcher

& Hunt (1998). This analysis assumes that the surface layer – which selects z_0 , viscous or not – has thickness much smaller than δ_i , and is valid for both the hydrodynamically rough and smooth regimes. In the long wave limit $kz_0 \ll 1$ where the inner layer thickness δ_i is much smaller than the wavelength, i.e. when $\ln(\delta_i/z_0) \gg 1$, the two-layer structure is recovered as sketched in Fig. 3c (left): an outer layer where the disturbed flow is dominated by inertia (green) and an inner layer dominated by Reynolds stresses (blue). From the balance of longitudinal advection and the turbulent stresses as given by the Prandtl mixing layer theory, the thickness δ_i of the inner layer is given from the implicit relation

$$\frac{\delta_i}{\lambda/4} \ln(\delta_i/z_0) = 2\kappa^2 \quad (9)$$

(another expression has been proposed which involves the square of the logarithm and provides smaller δ_i). From the matching of the outer and inner flows, the shear stress components \mathcal{A} and \mathcal{B} are found to be (Hunt et al. 1988, Kroy et al. 2002, Weng et al. 1991):

$$\mathcal{A} + i\mathcal{B} = 2 \frac{U^2(\delta_m)}{U^2(\delta_i)} \left(1 + \frac{1 + 2 \ln(\pi/2) + 4\gamma_E + i\pi}{\ln(\delta_i/z_0)} \right), \quad (10)$$

where U is the logarithmic velocity profile (1), $\gamma_E \simeq 0.577$ is Euler's constant and $\delta_m = (\lambda/4z_0) \ln^{-1/2}(\lambda/4z_0)$. Figure 3a-b shows that these asymptotic expressions (dashed blue lines) are valid for $kz_0 \lesssim 10^{-5}$.

The bottom shear stress has never been measured so far in the turbulent regime, so that only indirect determinations of \mathcal{A} and \mathcal{B} can be obtained from velocity measurements in the inner layer, assuming that the log velocity profile locally holds. As shown in Figure 3, they reasonably match the predictions (blue symbols). Besides, these velocity measurements confirm the linear increase of the mixing length with the distance to the bottom (Poggi et al. 2007). As shown

numerically by Ayotte et al. (1994), the predictions for the inner layer (\mathcal{A} and \mathcal{B} in particular) are robust to a change of the turbulence closure scheme: mixing length schemes (Colombini 2004, Fourrière et al. 2010, Mason & King 1985), models with equations for the turbulent kinetic energy and true second order closures (Finnigan et al. 1990, Weng et al. 1991)). Since the time-scale over which turbulent fluctuations adapt to the shear rate scales as δ_i/u_* in the inner layer, out-of-equilibrium turbulence effects vanish as $\ln^{-1}(\delta_i/z_0)$.

On the other hand, in the outer layer, the flow disturbance depends significantly on the closure law, especially Reynolds stresses. Second-order closures have revealed the influence of the lag between production and dissipation of turbulent fluctuations, related by Finnigan et al. (1990) to streamline curvature effects. This results into a *phase-lag* of the shear stress with respect to the topography (van Boxel et al. 1999, Walker & Nickling 2003, Weng et al. 1991, Wiggs et al. 1996) which contrasts with the *phase advance* in the inner layer. The second important effect in the outer layer is the rapid distorsion of turbulence by the mean shear, which results into Reynolds stress anisotropy (Ayotte et al. 1994, Finnigan et al. 1990).

2.2.4 TRANSITIONAL REGIME. Most of the measurements of \mathcal{A} and \mathcal{B} reported in Figure 3 have been obtained by Zilker et al. (1977) and Frederick & Hanratty (1988) (green points), and fall in the range $10^{-5} < kz_0 < 10^{-3}$ (green regions in all the figures). They clearly disagree with the calculations performed with a simple mixing-length closure (red curve). For this range of kz_0 , the perturbation partly penetrates into the turbulent region so that neither viscosity effects nor turbulent fluctuations can be neglected. On the upstream face of a bump where the flow is accelerated, the more negative streamwise pressure

gradient tends to damp the turbulent fluctuations so that the viscous sublayer thickens, whereas the opposite is true on the lee side. This results into a periodic transition from viscous to turbulent inner layer (see schematics in Figure 3c). Following Abrams & Hanratty (1985) and Frederick & Hanratty (1988), this effect can be accounted for by a dependence of the van Driest number α in (3) on the pressure gradient, with a space lag of the order of $\alpha^3\delta_\nu$ (from the classical argument for the thickening of a boundary layer, see the Online Supplementary Material). The prediction of this ‘Hanratty’s model’ is shown in Figure 3a,b (black solid line), and nicely fits the measurements. The modulation effect is resonant for wavenumbers $k\delta_\nu \approx 2\pi/\alpha^3 \approx 10^{-3}$, hence the large effect on \mathcal{A} and \mathcal{B} in the vicinity of this value. Although this model provides a convenient parametrisation, a true understanding of the interplay between a wavy bottom and the modulation of the viscous sublayer remains to be achieved.

2.2.5 PHYSICAL MECHANISM OF THE PHASE LAG BETWEEN SHEAR STRESS AND TOPOGRAPHY. The most important result of the above analyses is that \mathcal{A} and \mathcal{B} are both positive, so that the shear stress maximum is generically located upstream of the crest. The physical mechanism of this phase advance can be understood as follows. In the outer layer where the flow perturbation is essentially inviscid and potential (unlike the base state), the flow accelerates upstream of crests and slows down downstream, with opposite variation of the pressure (Bernoulli effect). This pressure also drives the flow in the inner layer, but there, bottom friction opposes the velocity variations. Because of fluid inertia, the variation of the shear stress must drive that of the fluid velocity, hence the positive phase advance. For a more quantitative discussion in the laminar regime, see Charru & Hinch (2000). As discussed in the following sections, this phase

advance is responsible for the instability of an erodible bed.

2.3 Beyond the linear response

For sinusoidal bottom with slope $k\zeta_0 \simeq 0.1$ (Kuzan et al. 1989), hydrodynamical nonlinear effects are no longer negligible. Harmonics grow and the phase advance of the shear stress reduces (Figure 2a-b) (Richards & Taylor 1981). Most numerical simulations (RANS, LES, DNS) and experiments in water have been performed in the transitional regime (Buckles et al. 1984, Cherukat et al. 1998, de Angelis et al. 1997, Frederick & Hanratty 1988, Henn & Sykes 1999, Zilker & Hanratty 1979), where the linear regime itself is not well understood as discussed above. In the simpler turbulent regime, qualitative aspects of the nonlinear hydrodynamical response have been understood, from field observations, wind tunnel experiments and numerical simulations over both sinusoidal bottom and isolated bumps (Buckles et al. 1984, Finnigan et al. 1990, Gong & Ibbetson 1989, Gong et al. 1996, Salvetti et al. 2001, Taylor et al. 1987, Yue et al. 2006, Zilker & Hanratty 1979). The linear asymptotic theory of Hunt et al. (1988) still predicts the dominant features of the flow (Belcher & Hunt 1998). On the upstream side of bumps, vertical profiles of the speed-up remain correctly described. By contrast, on the lee side, Prandtl mixing-length model fails to describe the flow and more elaborated closures schemes are necessary there (Ross et al. 2004, van Boxel et al. 1999).

On erodible beds, the initial sinusoidal topography also deforms and becomes asymmetric, while the height-to-length ratio tends to 1/15, approximately, for mature subaqueous ripples and aeolian dunes (Baddock et al. 2007, Parteli et al. 2006). An avalanche slip face develops on the lee side, from which the mean

flow separates and a recirculation bubble forms. From the coupling between hydrodynamics and erosion-deposition, the instability saturates, and the sand flux and elevation profiles vary in phase (Figure 6c).

From the theoretical point of view, the main difficulty is the quantitative description of flow separation, which, for sinusoidal bottom, occurs for $k\zeta_0 \gtrsim 0.3$ (Buckles et al. 1984, Finnigan et al. 1990, Henn & Sykes 1999, Zilker & Hanratty 1979). Aside from studies based on the triple-deck theory (Lagrée 2003), heuristic linear calculations have been proposed, of the turbulent flow above a fictive obstacle made of the true obstacle prolonged by the separation streamline (Finnigan et al. 1990, Jensen & Zeman 1985). However, separation is associated with the development of complex turbulent structures. An inflexion point appears in the mean velocity profile, corresponding to the formation a free shear layer. Spanwise vortices develop due to Kelvin-Helmholtz instability, which vortices then impinge the bottom near the reattachment point. Downstream of this point, very large velocity gradients take place close to the wall, associated with large shear stress (Figure 2b), and followed by the formation of longitudinal streaks and hair-pin vortices. When the reattachment length is larger than the wavelength, the free shear layer spreads and rises, while a new free shear layer is created downstream of the next crest, resulting in large production of turbulence and strong mixing of momentum. Large-scale streamwise vortices emerge with spanwise wavelength scaling on the streamwise wavelength of the bottom (Hudson et al. 1996, Kruse et al. 2003).

A complete description of the nonlinear response is definitely beyond the present review and remains a major challenging issue. A promising direction is weakly nonlinear analysis, following the studies of (Bordner 1978, Caponi et al. 1982,

Valance 2011) and (Andreotti et al. 2009, Colombini & Stocchino 2008) in the laminar and turbulent regimes (the coupling with the neutral mode $k = 0$, arising from (11), has not been included in the analysis yet). Another possible direction is the development of the triple-deck theory for turbulent flow.

3 The scales of particle transport

The observed modes of transport can be associated with the different forces acting on the particles. When the hydrodynamic forces exceed some threshold value related to the bed disorder at the particle scale (a fraction of the immersed weight $(\rho_p - \rho_f)gd^3$), the particles at the bed surface are set into motion. When the particles and the fluid have comparable densities (typically sand grains in water), the moving particles roll and slide on each other within a thin layer, of a few diameters thick, which mode of transport is called bedload. Lubrication forces are responsible for the dissipation. Conversely, for large ratio ρ_p/ρ_f (typically sand grains in air), the grains experience large jumps and the transport mode is called saltation. Dissipation is mainly due to the collisions of the moving particles with the bed. Finally, when the fluid velocity fluctuations, of magnitude u_* , become comparable with the settling velocity V_{fall} , of the order of $\sqrt{(\rho_p/\rho_f - 1)gd}$, grains are dispersed throughout the whole fluid layer, which mode of transport is called suspension.

3.1 What is the hydrodynamic parameter controlling transport?

The spatio-temporal evolution of the bed profile $\zeta(x, t)$, which is our primary interest, is related to the particle flux per unit width, $q(x, t)$, through the mass

conservation equation

$$\phi_b \frac{\partial \zeta}{\partial t} = -\frac{\partial q}{\partial x}, \quad (11)$$

where $\phi_b \approx 0.6$ is the volume fraction of the bed. Transport models aim at relating the flux q to the fluid flow. They are usually calibrated in homogeneous and steady situation controlled by one single hydrodynamic parameter: the bed shear stress τ , or equivalently the shear velocity u_* . The resulting particle transport is characterized by the so-called saturated flux $q_{\text{sat}}(\tau)$. Due to the trapping of the particles by gravity, q_{sat} vanishes below a threshold value $\tau_{\text{th}} = \rho_f u_{\text{th}}^2 \sim (\rho_p - \rho_f)gd$ which is sensitive to the geometrical disorder of the granular bed (Charru et al. 2004). Introducing the Shields number $\Theta = \tau/[(\rho_p - \rho_f)gd]$, dimensional analysis gives the general form of the transport law as

$$q_{\text{sat}} = u_s d \mathcal{Q}(\Theta), \quad (12)$$

where u_s is a characteristic velocity. The usual choice for u_s is the characteristic settling velocity $\sqrt{(\rho_p/\rho_f - 1)gd}$, but models based on the balance of horizontal momentum rather bring $u_s = u_{\text{th}}$. The dimensionless function \mathcal{Q} depends, in addition to Θ , on the density ratio ρ_p/ρ_f , which controls in particular the transition from bedload to saltation, and the settling Reynolds number $Re_s = V_{\text{fall}}d/\nu$ (or equivalently the threshold Reynolds number $Re_{\text{th}} = u_{\text{th}}d/\nu$), which controls the hydrodynamical regime at the grain scale.

When the bed topography is modulated by bedforms, the shear stress and particle flux are no longer uniform. This raises two issues. First, does the saturated transport law still hold? Early investigations have assumed local saturation of the sediment transport, with the local flux $q = q_{\text{sat}}(\tau)$ controlled by the local shear stress τ . However, there is experimental evidence that transport does not adapt instantaneously to a spatial change of the shear stress (Anderson & Haff

1988). As an illustration, Figure 4a displays the spatial relaxation of the flux towards saturation downstream of the transition between a non-erodible bottom ($x < 0$) and an erodible bed ($x > 0$), in the aeolian case, whereas Figure 4b displays similar results for suspension. However, over bedforms, the transport is never far from its saturated state, so that it can be described by a first-order linear relaxation in space and time:

$$T_{\text{sat}} \frac{\partial q}{\partial t} + L_{\text{sat}} \frac{\partial q}{\partial x} = q_{\text{sat}} - q, \quad (13)$$

where L_{sat} and T_{sat} are called the saturation length and times (Andreotti et al. 2002, Charru 2006, Claudin et al. 2011, Narteau et al. 2009, Parker 1975, Sauermann et al. 2001). Regarding ripples and dunes, the first term of this equation can be safely neglected, since T_{sat} is usually much smaller (~ 1 s) than the bedform growth time ($\sim 10^2$ s for subaqueous ripples and $\sim 10^5$ s for aeolian dunes). This separation of times justifies the simplifying assumption that the fluid flow can be computed as if the bed were fixed. The physical significance of L_{sat} is discussed below.

Second issue, at which vertical location should the shear stress be evaluated? As discussed in the previous section, τ can exhibit large vertical gradients in the outer layer, so that the question deserves attention. The usual approach uses $\tau(z = \zeta(x, t))$, which is a rigorous approximation when the transport layer, of thickness δ_t , is much thinner than the inner layer (typically, $\delta_t \approx d \approx 10^{-1} \delta_i$ in water close to threshold, and $\delta_t \approx \frac{\rho_p}{\rho_f} d \approx 10^{-2} \delta_i$ in air). An alternative approach has been proposed by Colombini (2004), which evaluates the shear stress at the distance $z = \zeta(x, t) + \delta_t$. Although appealing, this approach amounts to consider that the transport layer behaves as pure fluid, which is clearly not the case. Further investigation is needed here, accounting for the two-phase nature of the

transport layer and the shear-stress gradient in which the latter is embedded.

3.2 Linear response of the saturated flux

Eq. (13) describes the linear response of the flux q to a change of the saturated flux q_{sat} . To complete the description of transport on bedforms, one needs the linear response of q_{sat} to a small change $\delta\tau$ of the shear stress τ , and to a small change $s = \partial_x\zeta$ of the local bed slope from the horizontal. The response to $\delta\tau$ can be written $(\phi_b Q/\tau)\delta\tau$ where Q is the susceptibility with respect to the shear stress:

$$Q = \frac{\tau}{\phi_b} \left. \frac{\partial q_{\text{sat}}}{\partial \tau} \right|_{\tau} \quad (14)$$

As gravity tends to entrain particles downwards, a slope induces an additional contribution to the flux $-\mathcal{S}Qs$, where \mathcal{S} is the susceptibility with respect to the slope:

$$\mathcal{S} = -\frac{1}{Q} \left. \frac{\partial q_{\text{sat}}}{\partial s} \right|_{s=0}. \quad (15)$$

For $q \propto (\tau - \tau_{\text{th}})^n$ and with the assumption that the slope effect can be embedded in the change of the transport threshold, $\delta\tau_{\text{th}}/\tau_{\text{th}} = s/\mu$ where μ is an effective friction coefficient, one obtains $\mathcal{S} = \frac{1}{\mu}\tau_{\text{th}}/\tau$. Experiments give $\mu \simeq \tan 37^\circ$ in tilted wind tunnels (Iversen & Rasmussen 1999), and, for bedload in water, $\mu \simeq \tan 35^\circ$ (Dey 2003, Fernandez Luque & van Beek 1976) or $\mu \simeq \tan 65^\circ$ (Loiseleux et al. 2005), values consistent with the avalanche angle. Finally, \mathcal{S} typically decreases from ≈ 1.6 at the transport threshold to zero at large flow velocity.

3.3 What are the dynamical mechanisms controlling sediment transport?

The scaling laws followed by q_{sat} , L_{sat} and z_0 depend on the dynamical mechanisms controlling transport. We shortly review the results obtained for the three modes of transport.

3.3.1 BED LOAD IN WATER. The physical explanation proposed by Bagnold (1956) for the equilibrium bedload transport in the turbulent case is as follows. The moving particles are confined within a thin transport layer of thickness $\delta_t \simeq d$ and have a mean velocity $u_p \propto u_* - \beta u_{\text{th}}$, where $\beta < 1$ characterizes the effective bed friction. Across the transport layer, the fluid transmits momentum to the particles in proportion to the number n of mobile grains per unit surface. The equilibrium transport corresponds to the fluid shear stress being reduced to threshold at the fixed bed, which leads to $n \propto u_*^2 - u_{\text{th}}^2$. As the flux is $q = nu_p$, one gets $\mathcal{Q} \sim (\Theta - \Theta_{\text{th}})(\sqrt{\Theta} - \beta\sqrt{\Theta_{\text{th}}})$. The scaling of the sediment flux with the third power of the shear velocity, for large $\Theta/\Theta_{\text{th}}$, has been recovered in most experiments (Bagnold 1956). For viscous bedload, similar arguments give $\mathcal{Q} \propto \Theta^3$ (Bagnold 1956, Charru & Mouilleron 2002, Leighton & Acrivos 1986, Mouilleron et al. 2009, Ouriemi et al. 2009), while erosion-deposition models for a monolayer of particles, close to threshold, rather lead to $\mathcal{Q} \propto \Theta^2$ (Charru & Hinch 2006a).

The saturation transient may be controlled by two mechanisms: the erosion or deposition of particles (related to the relaxation of n), or particle inertia (relaxation of u_p). For bedload, Charru & Hinch (2006a) proposed that erosion and

deposition are the limiting processes, which leads to the saturation length

$$L_{\text{sat}} \propto \frac{U}{V_{\text{fall}}} d \quad (16)$$

where U is the fluid velocity at the particle scale and d/V_{fall} is the typical time needed for one particle to settle. Therefore, L_{sat} scales on a deposition length (Lajeunesse et al. 2010). However, L_{sat} has never been measured directly for bedload, unlike for saltation and suspension.

As mentioned in the previous section, bedload transport may change the hydrodynamical roughness z_0 seen from the inner layer. The measurements collected by van Rijn (1982) show $z_0 = 1 - 10 d$, which is significantly larger than for a fixed bed; Richards (1980) uses the empirical result that z_0/d increases linearly with Θ . A thorough assessment of these laws remains to be performed. Beside, in the transitional regime, transport may affect the modulation of the viscous sublayer.

3.3.2 SALTATION IN AIR. The stress balance still holds for saltation, and the scaling of n is the same as above (Owen 1964). However, the particle motion takes place over a much thicker layer, $\delta_t \simeq (\rho_p/\rho_f)d \gg d$, in which, contrarily to bedload, the wind velocity is strongly reduced due to the large particle inertia (Andreotti 2004, Ungar & Haff 1987). The entrainment of new grains mostly result from collisions. The balance between erosion and deposition implies that the mean grain velocity u_p is a constant, scaling with u_{th} . The resulting scaling law $\mathcal{Q} \sim (\Theta - \Theta_{\text{th}})$ is in agreement with wind-tunnel experiments (Creyssels et al. 2009, Iversen & Rasmussen 1999), but contrasts with the initial proposition of Bagnold (1941) and followers.

The saturation transient is limited by particle inertia, so that the saturation length L_{sat} scales with the length needed for one grain to be accelerated up to

the wind velocity (Andreotti et al. 2010, Hersen et al. 2002):

$$L_{\text{sat}} \propto \frac{\rho_p}{\rho_f} d. \quad (17)$$

L_{sat} is therefore independent of u_* and is of the order of one meter, as confirmed by direct measurements (Figure 4a). Note that the initial exponential increase of the sand flux that can be seen in the figure for $q \ll q_{\text{sat}}$, is due to erosion and takes place over a distance decreasing as u_*^{-2} (Sauermann et al. 2001).

Experiments (Iversen & Rasmussen 1999) and models (Andreotti 2004, Durán et al. 2011) agree on the large increase of the hydrodynamical roughness z_0 with the density of mobile grains, and therefore with u_* . It provides a direct proof of the strong negative feedback, inside the transport layer, of the particles on the fluid velocity.

3.3.3 SUSPENSION. In the suspension regime ($u_* \gtrsim V_{\text{fall}}$), particles diffuse over the whole water depth D , and the particle flux results from the balance between upwards diffusion and sedimentation. Experiments (Ashida & Okabe 1982, Jobson & Sayre 1970, van Rijn 1986) and theoretical analysis (Claudin et al. 2011) have shown that the saturation length then scales as

$$L_{\text{sat}} \propto \frac{U}{V_{\text{fall}}} D, \quad (18)$$

i.e. on a deposition length based on the depth-averaged flow velocity U and the settling time D/V_{fall} (Figure 4b). This law is the same as for bedload, expect that the length over which the grains settle now scales with the flow depth D rather than the grain diameter. As $D/d \gg 1$, L_{sat} can be very large: several meters in flume experiments and hundreds of meters in natural rivers.

4 Stability analysis of a flat erodible bed

The question of the instability of an erodible bottom is now addressed by putting together the previous analyses of the fluid flow (§2) and particle transport (§3). The instability mechanism is shown to arise from the hydrodynamics, for both subaqueous ripples and aeolian dunes, while gravity and sediment transport are stabilizing. Unbounded flow is still considered here as the reference case.

4.1 Dispersion relation

As clearly recognized by Kennedy (1963, 1969), a crucial feature at the origin of the growth of a sinusoidal disturbance of an erodible bed is the phase lead of the perturbation τ_b of the bed shear stress, as given by Eq. 5. Let $\zeta(x, t) = \zeta_0 e^{\sigma t} \cos(kx - \omega t)$ be the slowly varying bed disturbance. The component of τ_b in quadrature with $\zeta(x, t)$ (proportional to $\mathcal{B} > 0$) drags the particles from troughs to crests, amplifying the initial bed disturbance (positive growth rate σ), whereas the in-phase component (proportional to $\mathcal{A} > 0$) is responsible for the downstream migration of the disturbance, with phase velocity $c = \omega/k$. We discuss here the dispersion relation, i.e. the dependence of σ and c on the wavenumber k .

4.1.1 STABILIZING EFFECTS IGNORED. We first ignore the stabilizing slope effect ($\mathcal{S} = 0$) and consider that particle transport q is at local equilibrium with the shear stress ($L_{\text{sat}} = 0$). Then, as $q = q_{\text{sat}}(\tau)$, the amplitude of the flux disturbance is $\hat{q} = \phi_b Q (\mathcal{A} + i\mathcal{B}) k \zeta$ with Q defined by Eq. 14. The bed evolution is governed by the particle mass conservation equation (Eq. 11) and the dispersion relation follows as

$$\sigma = \mathcal{B}(kz_0) Q k^2, \quad c = \mathcal{A}(kz_0) Q k. \quad (19)$$

Since fluid inertia imposes $\mathcal{B} > 0$ for any wavenumber (Figure 3b), all wavenumbers are amplified (Figure 5a). Some stabilizing processes must be at work to get some wavenumber selection.

4.1.2 SLOPE EFFECT. Introducing the slope effect, \hat{q}_{sat} becomes

$$\hat{q}_{\text{sat}} = \phi_b Q [\mathcal{A}(kz_0) + i(\mathcal{B}(kz_0) - \mathcal{S})] k\zeta. \quad (20)$$

The additional \mathcal{S} -term does not provide any new length scale but reduces the growth rate from $Q\mathcal{B}k^2$ to $Q(\mathcal{B} - \mathcal{S})k^2$. As $\mathcal{B}k^2$ tends to the constant value $\frac{1}{2}\delta_\nu^{-2}$ at large k (§2), the slope effect stabilizes short waves: instability is suppressed beyond some cut-off wavenumber (Figure 5a) (Fredsoe 1974). The slope effect is expected to be significant close to the transport threshold Θ_{th} and become negligible farther as \mathcal{S} decreases with increasing shear stress (§3).

4.1.3 TRANSPORT RELAXATION. For spatially varying shear stress, the adjustment of the particle flux is not instantaneous but takes place over some relaxation length L_{sat} (§3). According to Eq. 13, the amplitudes of the actual and saturated flux disturbances, \hat{q} and \hat{q}_{sat} , are then related by $(1 + ikL_{\text{sat}})\hat{q} = \hat{q}_{\text{sat}}$, so that the growth rate and wave velocity become

$$\sigma = Qk^2 \frac{(\mathcal{B} - \mathcal{S}) - \mathcal{A}kL_{\text{sat}}}{1 + (kL_{\text{sat}})^2}, \quad c = Qk \frac{\mathcal{A} + (\mathcal{B} - \mathcal{S})kL_{\text{sat}}}{1 + (kL_{\text{sat}})^2}. \quad (21)$$

We see that transport relaxation brings a stabilizing term in the growth rate when $\mathcal{A} > 0$, which dominates at large wavenumber (Figure 5a). Thus, transport relaxation stabilizes short waves, like the slope effect.

4.2 Linear wavelength selection

The most unstable mode is expected to correspond to the observed wavelength emerging from an initially flat bed, at least for short times when nonlinear effects

are still negligible. We discuss here the competition of the mechanisms at work for the selection of this mode, which involves a hydrodynamical length scale (the inner layer thickness δ_i or the roughness length z_0), the transport relaxation length L_{sat} , and the dimensionless slope parameter \mathcal{S} .

4.2.1 ZERO L_{sat} . Ignore first the transport relaxation, so that only the slope effect may counteract the destabilizing fluid inertia. The most unstable wavenumber is nearly proportional to the cut-off wavenumber k_c , which is solution of $\mathcal{B}(k_c z_0) = \mathcal{S}$ according to Eq. 21 and can be obtained graphically from Figure 3. Using the asymptotic expression Eq. 8 for \mathcal{B} (laminar inertial regime), a good estimate of the most amplified wavelength is found as (Charru & Mouilleron 2002)

$$\lambda = 2\pi \frac{3\mathcal{S}}{\gamma_L} \delta_i \quad \text{or} \quad \lambda = 2\pi \left(\frac{3\mathcal{S}}{\gamma_L} \right)^{3/2} \delta_\nu. \quad (22)$$

The full calculation in the smooth hydrodynamical regime (Figure 3b) confirms this scaling with the hydrodynamical length δ_ν (Sumer & Bakioglu 1984).

Using the measured values of \mathcal{S} (§3), the predicted wavelength in water is found to be much smaller, by one order of magnitude at least, than measured wavelengths (Figure 5a). Large values of \mathcal{S} , likely unrealistic, are necessary to reduce the discrepancy (e.g. $\mathcal{S} = 2.8$ used by Richards (1980)). For aeolian dunes, the mismatch reaches three orders of magnitude. The conclusion is that, although some uncertainties remain on the values of \mathcal{S} , the slope effect alone is not stabilizing enough.

4.2.2 NONZERO L_{sat} . Figure 5b displays the most unstable wavelength λ/L_{sat} as a function of L_{sat}/z_0 , calculated from Eq. 21 for the three hydrodynamical models discussed in Section 2. When the saturation length is small compared to the hydrodynamical length, say $L_{\text{sat}} < 10 z_0$, it appears that the selected wave-

length is essentially controlled by the hydrodynamics, which is in the laminar regime. In particular, for nonzero \mathcal{S} , the scaling Eq. 22 is recovered.

For large L_{sat}/z_0 and $\mathcal{S} = 0$, Figure 5b shows that λ/L_{sat} is nearly constant and in the range 15–30, which means that λ scales approximately on L_{sat} . In the hydrodynamically rough regime (blue solid line), this result can be understood from the fact that for $kz_0 \ll 1$, \mathcal{A} and \mathcal{B} depend weakly –logarithmically– on kz_0 and can be considered as constants and evaluated at z_0/L_{sat} . Then, the most amplified wavenumber is expected to scale on the cut-off wavenumber k_c defined by $\mathcal{B}(k_c z_0) = \mathcal{A}(k_c z_0) k_c L_{\text{sat}}$, i.e. the balance of destabilizing fluid inertia and stabilizing particle relaxation. This analysis finally gives (Andreotti et al. 2002)

$$\lambda \propto \frac{\mathcal{A}(z_0/L_{\text{sat}})}{\mathcal{B}(z_0/L_{\text{sat}})} L_{\text{sat}}. \quad (23)$$

In the hydrodynamically smooth regime (red and black lines), the above scaling is recovered but at larger L_{sat}/z_0 ($> 10^4$), i.e. in the turbulent regime. For smaller L_{sat}/z_0 in the range $10^1 - 10^4$, i.e. in the more complicated transitional regime (green area), the selected wavelength depends on both z_0 and L_{sat} .

The slope effect parametrized by \mathcal{S} induces a further stabilizing effect, which results in larger wavelengths (dashed lines in Figure 5b). When $\mathcal{S} > \mathcal{B}(kz_0)$ for all wavenumbers, the flat bed is stable (at the right of the dots ending the dashed lines). This situation is more likely to happen close to the transport threshold where the slope effect is stronger, and in the turbulent regime where \mathcal{B} decreases below $\mathcal{S} = 1.6$. Farther from threshold, \mathcal{S} decreases and long waves become unstable.

4.2.3 AEOLIAN DUNES. The best understood situation is that of aeolian dunes, for which wind tunnel experiments have provided measurements of q_{sat} , L_{sat} , \mathcal{S} and z_0 (e.g. Andreotti et al. (2010), Creyssels et al. (2009), Ho et

al. (2011), Iversen & Rasmussen (1999). Aeolian transport takes place in the turbulent regime for which hydrodynamical calculations are robust with respect to turbulent closures and lead to nearly constant \mathcal{A} and \mathcal{B} (Figure 3). Moreover, the different lengths of the problem are well separated (Table 1). Figure 6c displays the development of dunes on the flank of large barchans (Elbelrhiti et al. 2005). In this situation, L_{sat} is the relevant length scale and Eq. 23 holds. The slope effect changes Eq. 23 to $\lambda \propto \frac{\mathcal{A}}{\mathcal{B}-\mathcal{S}}L_{\text{sat}}$, which predicts an increase of λ close to the transport threshold, in agreement with observations (Figure 6d) (Andreotti et al. 2010).

The proportionality of the saturation length with the drag length $(\rho_p/\rho_f)d$ (Figure 4b) may be assessed by the comparison of dune sizes in different environments. In particular, it explains why on Mars, where the atmosphere is significantly lighter than on Earth, dunes have wavelengths ten times larger (Claudin & Andreotti 2006). Conversely, aeolian features that emerge under high pressure CO_2 are on the decimeter scale (Greeley et al. 1984). As for the growth rate $\sigma \sim L_{\text{sat}}^2/Q$, its dependence on L_{sat}^2 may explain the apparent large-scale inactivity of Martian dunes, since it predicts very large growth time, typically centuries, in contrast to days on Earth. Recent observations of the propagation of small ripples confirm that Mars is active (Silvestro et al. 2010).

4.2.4 SUBAQUEOUS RIPPLES. The situation in liquids is less definite than in air, for the following reasons: (i) the separation of the length scales, δ_t , L_{sat} , z_0 and δ_i , is less pronounced (Table 1); (ii) no direct measurement of L_{sat} is available yet; (iii) the observed ripples lie at the transition between the laminar and turbulent regimes, more sensitive to the flow modeling (Figure 6b). Numerous experiments have been performed, with various particles, with a free surface or

an upper wall, but eventually exploring a rather limited range of the parameters (e.g., the grain Reynolds number d/δ_ν , and the distance to threshold u_*/u_{th}). Moreover, the focus is often on mature ripples rather than on the first stages of the instability.

Initial ripple wavelengths are typically in the range 100–800 d , both in water (Baas 1994, 1999, Betat et al. 1999, Coleman & Melville 1996, Fourrière et al. 2010, Langlois & Valance 2007) and in viscous fluids (Charru & Mouilleron 2002, Kuru et al. 1995). Figure 5a displays measured growth rates and a fit with Eq. 21 including both the slope effect and a (somewhat large) saturation length. Figure 6b displays measured wavelengths from the above references together with the most amplified mode computed from the three hydrodynamical models. It can be seen that subaqueous ripples form in the transitional regime (green shaded area) where the most amplified wavelength involves both L_{sat} and δ_ν . The general trend that emerges is the decrease of λ/d with d/δ_ν . Only Hanratty’s model reproduces the correct trend, with the saturation length fitted to $L_{\text{sat}} \simeq 12 \frac{U}{V_{\text{fall}}} d$, consistently with measurements of the deposition length by Lajeunesse et al. (2010).

The existence of an instability threshold larger than the transport threshold is consistent with the observation a ‘lower plane’ regime reported in bedform stability diagrams (Southard 1991). An ‘upper plane regime’ where the bedforms flatten and disappear is also reported in these diagrams, which generally corresponds to large particle Reynolds number, typically $d/\delta_\nu > 25$. This observation is accounted for by Sumer & Bakioglu (1984) with a shift of the mixing-length depending on the roughness. Another explanation could be that for large grains, the flow depth is relatively smaller, or that the transport layer thickens and the

saturation length becomes larger, which effects are stabilizing (§5).

4.3 Nonlinear coarsening

We now turn to nonlinear aspects, restricting the discussion to subaqueous ripples. Once the quasi-sinusoidal ripples have emerged from the flat bed, their height $H = 2\zeta_0$ first grows exponentially with time (Figure 7a) (Betat et al. 1999, Fourrière et al. 2010). Then nonlinear effects quickly arise: the profile becomes asymmetrical (inset in Figure 7a), and after a couple of minutes the ripple height saturates, while the wavelength remains unchanged. Then, on a much longer time scale (hours), the small velocity differences related to small height differences ($c \propto 1/H$, §1) lead to collisions and merging between adjacent ripples, see the spatio-temporal diagram in the inset of Figure 7b (Betat et al. 2002, Coleman & Melville 1994). This results in coarsening of the pattern and an increase of the averaged wavelength (Figure 7a). Eventually, λ saturates because of finite-size effects, see §5.

Most of the ripple lengths reported in the litterature correspond to mature nonlinear bedforms (Guy et al. 1966, Yalin 1985)), not linear waves. A selection of these measurements close to threshold ($u_* < 1.5 u_{\text{th}}$) is displayed in Figure 6d. Interestingly, they nearly fall on a straight line close to the edge of the transitional regime (the left edge in Figure 3), $k\delta_\nu \approx 3 \times 10^{-4}$.

5 Finite size effects

We now consider bounded flow, i.e. $kD \lesssim 1$, where the upper boundary, either a rigid wall (closed channels) or a free surface (open channels, rivers, stratified atmosphere), is expected to affect the bottom shear stress. Several new patterns

arise, such as subaqueous dunes, anti-dunes, chevrons and alternate bars, see the photos in Figure 8.

5.1 Hydrodynamics

For rigid upper boundary, the only new parameter is kD . As this parameter decreases, the inner layer progressively invades the whole flow. The sole effect of the confinement is to lower inertia, so that the in-quadrature shear stress component \mathcal{B} decreases, for both laminar and turbulent flows (Charru & Mouilleron 2002, Engelund 1970, Fourrière et al. 2010, Richards 1980).

For a free surface flow with surface velocity U , an additional parameter enters the analysis: the Froude number $Fr = U/\sqrt{gD}$ which measures the relative magnitude of inertia and gravity. The situation can be summarized as follows. For subcritical flow ($Fr < 1$), the confinement is still stabilizing: the in-phase shear stress component \mathcal{A} increases, while \mathcal{B} lowers and even becomes negative for $kD \ll 1$. The Saint-Venant equations, for instance, produce a negative \mathcal{B} (Gradowczyk 1968, Luchini & Charru 2010). For the more general case of 3D flow over a wavy bottom $\zeta = \zeta_0 \cos(k_x x) \cos(k_y y)$, only the component \mathcal{B}_x parallel to the main flow becomes negative, whereas the transverse component \mathcal{B}_y is enhanced (Andreotti et al. 2012). For supercritical flow ($Fr > 1$), the free surface is crucial when the surface waves resonate with the undulations of the bottom, which occurs in a narrow window in the diagram (Fr, kD) (Engelund 1970). The resonance induces a sharp decrease of \mathcal{B} , and also strongly affects \mathcal{A} which can become negative.

5.2 Linear instability and pattern formation

The linear stability analysis can be performed as before with \mathcal{A} and \mathcal{B} now encoding the finite- D effect. Sediment transport remains unchanged and essentially imposes the length scale L_{sat} . Different regimes are found, depending on the dimensionless ratio L_{sat}/D (Andreotti et al. 2012). For small L_{sat}/D and $Fr < 1$, the most unstable wavelength is not influenced by the free surface and remains as in the unbounded case (ripples). In particular, there is no secondary maximum to be associated with dunes. Experimental evidence (see Figure 7) strongly suggests that dunes emerge from the pattern coarsening of ripples (Coleman & Melville 1994, Fourrière et al. 2010, Raudkivi 2006, Raudkivi & Witte 1990) rather than by linear instability (Colombini 2004, McLean 1990, Richards 1980). The increase of the mean wavelength is stopped by the stabilizing role of the free surface at small kD , and λ eventually scales with D . In the aeolian case, the stratified structure of the atmosphere above deserts is qualitatively analogous to a river surrounded by air: the equivalent of the flow depth is the thickness of the convective boundary layer, capped by the thin inversion layer which plays the role of the free surface. This stratification, whose thickness varies by a factor of up to 5 from coastal to continental deserts, bounds the size of giant aeolian dunes (Andreotti et al. 2009).

For $L_{\text{sat}}/D \gtrsim 0.1$ and still subcritical flow, oblique bedforms with angle α with the flow direction are more unstable than transverse ones ($\alpha = 0$). This explains the generation, in shallow water, of rhomboid beach patterns or chevrons (the combination of two plane waves with angles α and $-\alpha$) (Daerr et al. 2003, Devauchelle et al. 2010, Morton 1978, Venditti et al. 2005). This also explains the oblique or alternate bars observed in flumes with coarse grains (Lanzoni 2000,

Lisle et al. 1991). Large values of L_{sat}/D are also reached when suspension is the dominant mode of transport (§3). Some alternate bars observed in flume experiments are in this regime (Chang et al. 1971), as well as the bars formed in rivers during floods, where most of the sediment is suspended. In rivers and flumes, the depth-to-width ratio D/W is a new control parameter, with the transverse wavenumber of bedforms being selected by the finite width. The braiding patterns observed for small D/W can be interpreted as high-order modes.

For supercritical Froude number ($Fr > 1$), the free surface now has a destabilizing effect associated with the change of sign of \mathcal{A} at the resonance. The growth rate of modes with $kD \simeq 1$ dominates that of ripples when $L_{\text{sat}} \gtrsim D$. This situation corresponds to large deformations of the free surface and anti-dunes propagating upstream (Kennedy 1969, Parker 1975). The range of unstable wavenumbers kD is so closely related to the resonance, and thus so narrow, that the most unstable mode is selected by the hydrodynamics, $\lambda \propto D$. Besides, anti-dunes hardly experience pattern coarsening.

Measured wavelengths corresponding to the patterns described above are displayed in the (Fr, kD) diagram of Figure 8. They gather in different groups. Anti-dunes nicely follow the resonant curve (red solid line), while dunes (and mega-dunes) lie in the subcritical unstable region.

6 Conclusion

6.1 Summary Points

1. The formation of subaqueous ripples and aeolian dunes in unbounded flow (bedform wavelength smaller than the flow depth) results from the destabilizing action of fluid inertia, which induces a phase advance of the shear

stress relative to the bed disturbance.

2. The most relevant hydrodynamical length is the thickness δ_i of the inner layer above which the dynamics of the flow disturbance is essentially inviscid and potential.
3. The destabilizing inertia is balanced by the stabilizing lag of the particle flux with respect with shear stress. The saturation length L_{sat} associated with this relaxation effect is an essential feature for the understanding of the instability. A second stabilizing effect is the bedform slope which drags the particles towards troughs.
4. For aeolian dunes, the scales of the problem are well separated, the initial dune wavelength is, as a first approximation, proportional to the saturation length, times the hydrodynamical factor \mathcal{B}/\mathcal{A} encoding the phase advance of the bed shear stress. The saturation length results from grain inertia and is proportional to the drag length $(\rho_p/\rho_f)d$. Weaker effects arise from the dependence of λ/L_{sat} to L_{sat}/z_0 and the slope parameter \mathcal{S} .
5. For subaqueous ripples, the conclusion is less clear-cut. Most of the experimental and field data lie in the transition between the laminar and turbulent regimes, where the bed shear stress is more sensitive to the turbulence modeling. However, there is direct evidence that ripples form by linear instability of a flat bed, and their initial wavelength, in the range 100–800 d , is consistent with L_{sat} in the range 10–30 d . The rapid coarsening of the pattern makes difficult the interpretation of many data from the literature.

6.2 Future issues

1. The laminar-turbulent transitional regime, in which most of the subaqueous ripples lie, remains to be understood. The effect on the bed shear stress of turbulent coherent structures in the near-bed region, notably longitudinal streaks, is largely unknown.
2. The nonlinear description of the hydrodynamical response to a complex relief remains to be completed, in particular, the secondary flows behind star dunes and other three-dimensional dunes.
3. The saturation length L_{sat} for bedload has to be measured and understood, as well as its large increase at the transition from bedload to suspension.
4. A quantitative nonlinear description of the asymmetry and saturated amplitude of dunes is open, as well as the description of dune interactions, collisions, coalescence and splitting, in one-dimensional channels and two-dimensional fields.
5. Finally, the effects of grain polydispersity and segregation have to be understood.

7 Side bar: oscillating ripples

The oscillatory motion of a liquid above a granular bed leads to the formation of ripples, as under steady flow (Rousseaux et al. 2004, Sleath 1976). The sand ripples one observes on a beach at low tide are an example: these ripples were formed by the oscillations induced by the surface waves when the beach was covered with shallow water. The mechanism of their formation, related to fluid inertia, is the same as that of ripples under steady flow, with positive phase

advance of the shear stress dragging the particles towards crests during each half-period (Blondeaux 1990, Charru & Hinch 2006b). The net particle flux towards crests can also be understood as the result of the mean steady drift flow (steady streaming). Similar structures are also observed on the continental shelf at water depths of two to three hundred meters, with a wavelength on the order of a meter. These ripples play an important role in attenuating the wave motion, essentially owing to dissipation in the oscillating boundary layer and vortex detachment from their peaks.

8 Key Terms and Definitions

- Barchan dune: crescentic-shaped dune migrating on a non-erodible ground, with horns pointing downstream.
- Star dune: large dune shaped like a star, with several arms originating from the crest; fairly stationary because of changing wind regimes.
- Aeolian ripple: centimeter scale bedform created by the impact on a sand bed of saltating grains entrained by the wind. The formation of these ripples, quite different from that of subaqueous ripples, is out of the scope of the present review.
- Subaqueous ripple: centimeter scale transverse bedform created by the steady water flow over an erodible bed.
- Subaqueous dune: large bedform whose size scales on the water depth.
- Oscillating ripples: subaqueous ripples created by oscillating flow.
- Antidune: subaqueous bedform propagating upstream in supercritical flow.
- Chevrons: subaqueous inclined (non-transverse) bedforms emerging in shal-

low flows.

- Alternate bars: non-transverse features forming in rivers and flumes, with size much larger than the flow depth.
- Saturation length: distance needed for non-equilibrium particle flux to relax towards its saturated value.
- Saturated flux: volume of particles transported per unit time and width, in equilibrium with the shear stress exerted by the fluid flow.

Table 1: Typical flow conditions and length scales for a sand bed under oil ($\nu = 10^{-5} \text{ m}^2 \text{ s}^{-1}$), water ($\nu = 10^{-6} \text{ m}^2 \text{ s}^{-1}$) and air ($\nu = 15 \times 10^{-6} \text{ m}^2 \text{ s}^{-1}$): friction velocity u_* , grain diameter d , particle Reynolds number d/δ_ν , typical wavelength λ , inner layer thickness δ_i , scale separation δ_i/δ_t (tr: transitional regime, tu: turbulent regime), kz_0 , Shields number θ and L_{sat}/d .

Fluid flow	u_* (m s^{-1})	d (mm)	d/δ_ν	λ (m)	δ_i (mm)	δ_i/δ_t	kz_0 $\times 10^3$	Θ	L_{sat}/d
Oil	0.02	0.1	0.2	0.1	1	5	3 (tr)	0.25	$\approx 20?$
Water	0.02	0.2	4	0.1	1.4	4	0.3 (tr)	0.12	$\approx 10?$
Air	0.4	0.2	5	50	500	50	0.03 (tu)	0.05	$\approx 10^4$

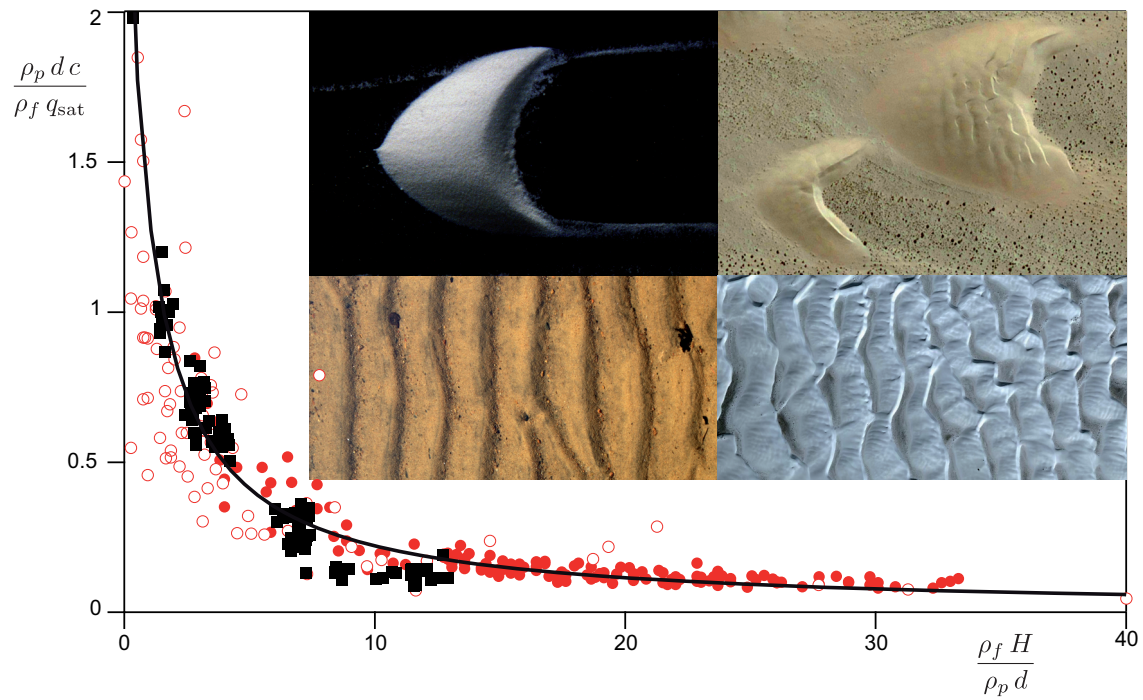


Figure 1: Migration velocity c of dunes as a function of their height H for aeolian barchan dunes (\bullet), dunes propagating on the back of large aeolian dunes (\circ) and subaqueous barchan dunes (\blacksquare). Solid line: Bagnold's prediction. Inset: photographs of barchan (top) and transverse (bottom) dunes formed under water (left) and air (right). Note the superimposed bedforms on the back of aeolian dunes.

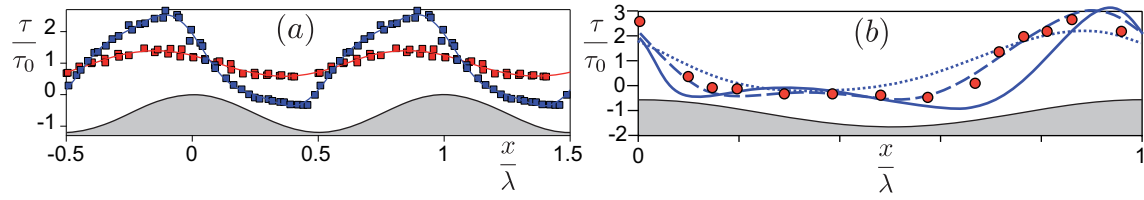


Figure 2: Bottom shear stress τ/τ_0 on a smooth sinusoidal bottom (black line).
 (a) Measurements for $2\zeta_0/\lambda = 0.0125$ (■) and 0.05 (■) (Zilker et al. 1977) and best fit with three harmonics (solid lines). (b) Measurements for $2\zeta_0/\lambda = 0.2$ (●) (Buckles et al. 1984) and large-eddy simulation for $2\zeta_0/\lambda = 0.0125$ (.....), 0.1 (---), and 0.2 (—) (Henn & Sykes 1999).

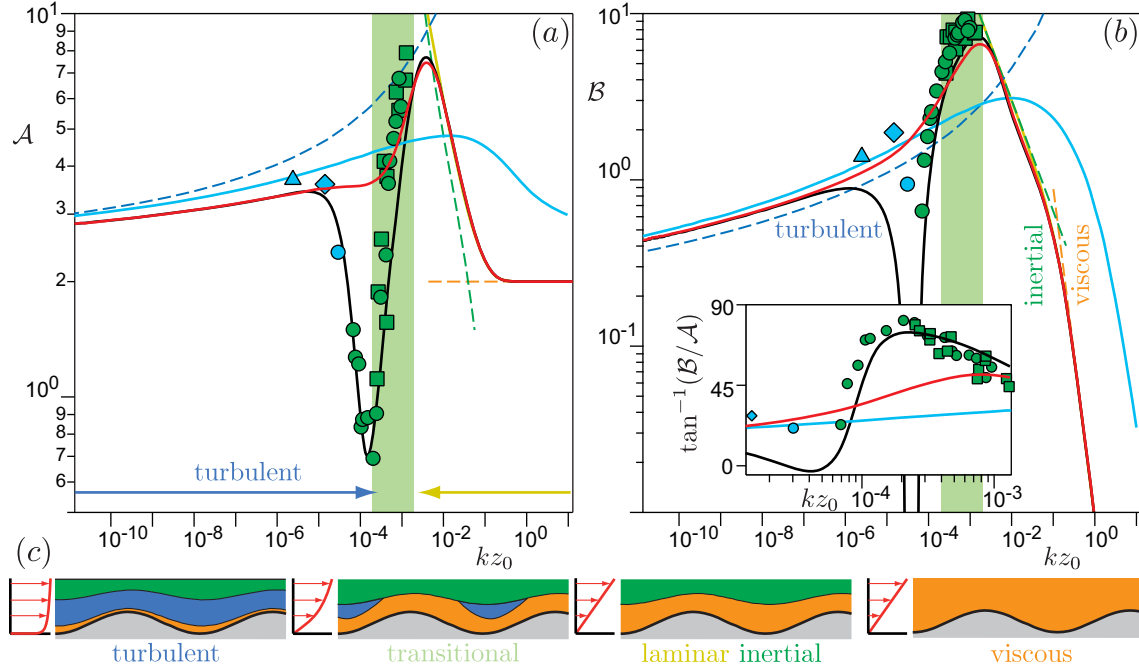


Figure 3: Shear stress components in-phase \mathcal{A} (a) and in quadrature \mathcal{B} (b) as a function of the wavenumber kz_0 . Inset: phase shift $\tan^{-1}(\mathcal{B}/\mathcal{A})$ in degrees. Solid lines: full calculations; dashed lines: asymptotic calculations. (—), smooth closure Eq. 3; (—), ‘Hanratty’s model’; (—), rough closure Eq. 4; (—), laminar Couette flow; (—), Eq. 10; (—), Eq. 7; (—), Eq. 8. Green region: transition between the laminar and turbulent regimes. ■, ●, from electrochemical measurements (Frederick & Hanratty 1988, Zilker et al. 1977). ▲, from velocity measurements on a 40 m long protodune. ◆, flume (Poggi et al. 2007). ●, flume (Finnigan et al. 1990). (c) Schematics of the layered structure of the disturbed flow in the different regimes.

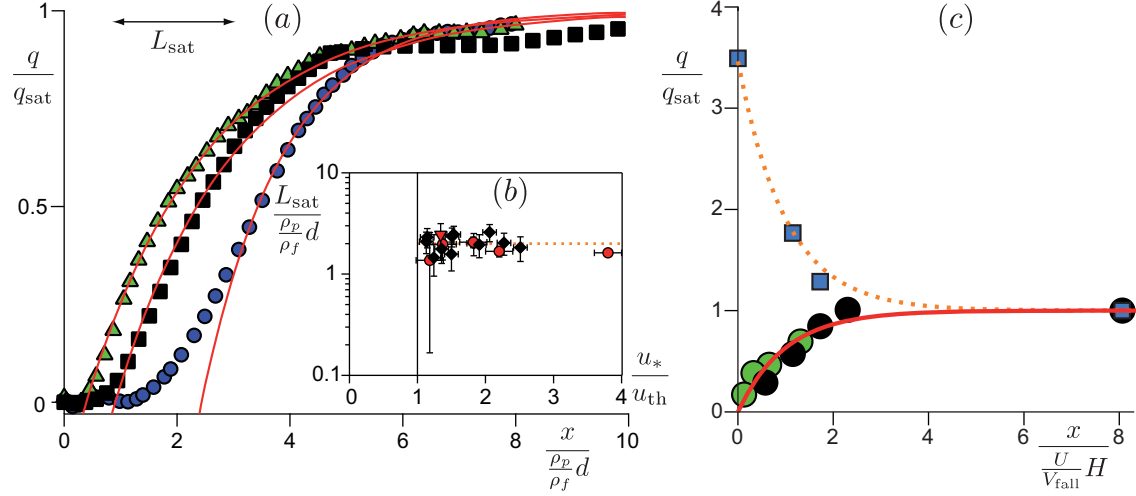


Figure 4: Relaxation of the sediment flux q towards q_{sat} ; (a), aeolian transport; (b), suspension. (a), The wind erodes a sand patch starting at $x/L_{\text{drag}} = 0$ with drag length $L_{\text{drag}} = \frac{\rho_p}{\rho_f}d$; \blacktriangle , $u_*/u_{\text{th}} \simeq 1.8$; \blacksquare , $u_*/u_{\text{th}} \simeq 1.5$; \bullet , $u_*/u_{\text{th}} \simeq 1.2$. Red lines: best exponential fits $q/q_{\text{sat}} = 1 - \exp(-x/L_{\text{sat}})$ (Andreotti et al. 2010). Inset: $L_{\text{sat}}/L_{\text{drag}}$ as a function of u_*/u_{th} . Black symbols: direct measurement from wind tunnel experiments; red symbols: indirect estimate from the analysis of dune initial wavelengths (field data); dotted line: $L_{\text{sat}} = 2(\rho_p/\rho_f)d \approx 0.8$ m. (b) Similar measurements for particles transported in suspension, with distance x rescaled by the deposition length $L_{\text{dep}} = (U/V_{\text{fall}})D$, for net erosion (\bullet , van Rijn (1986); \bullet , Ashida & Okabe (1982)) and net deposition (\blacksquare , Ashida & Okabe (1982)), along with exponential fits (solid and dotted lines).

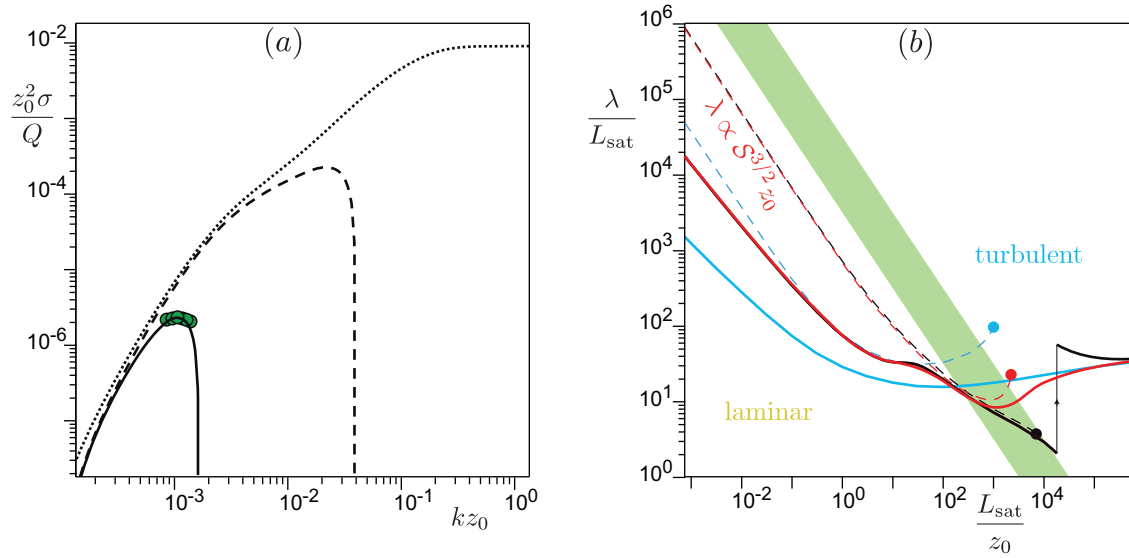


Figure 5: (a) Growth rate σ as a function of wavenumber kz_0 from Hanratty’s model, for $L_{\text{sat}} = 0$ and $\mathcal{S} = 0$ (dotted line), $L_{\text{sat}} = 0$ and $\mathcal{S} = 1.0$ (dashed line) and $L_{\text{sat}} = 90 \delta_\nu = 36 d$ and $\mathcal{S} = 1.0$ (black line). These latter values are chosen to fit measurements (●) from Betat et al. (1999). (b) Most unstable wavelength λ rescaled by L_{sat} computed for $\mathcal{S} = 0$ (solid lines) and $\mathcal{S} = 1.6$ (dashed lines). The color code is as in Figure 3.

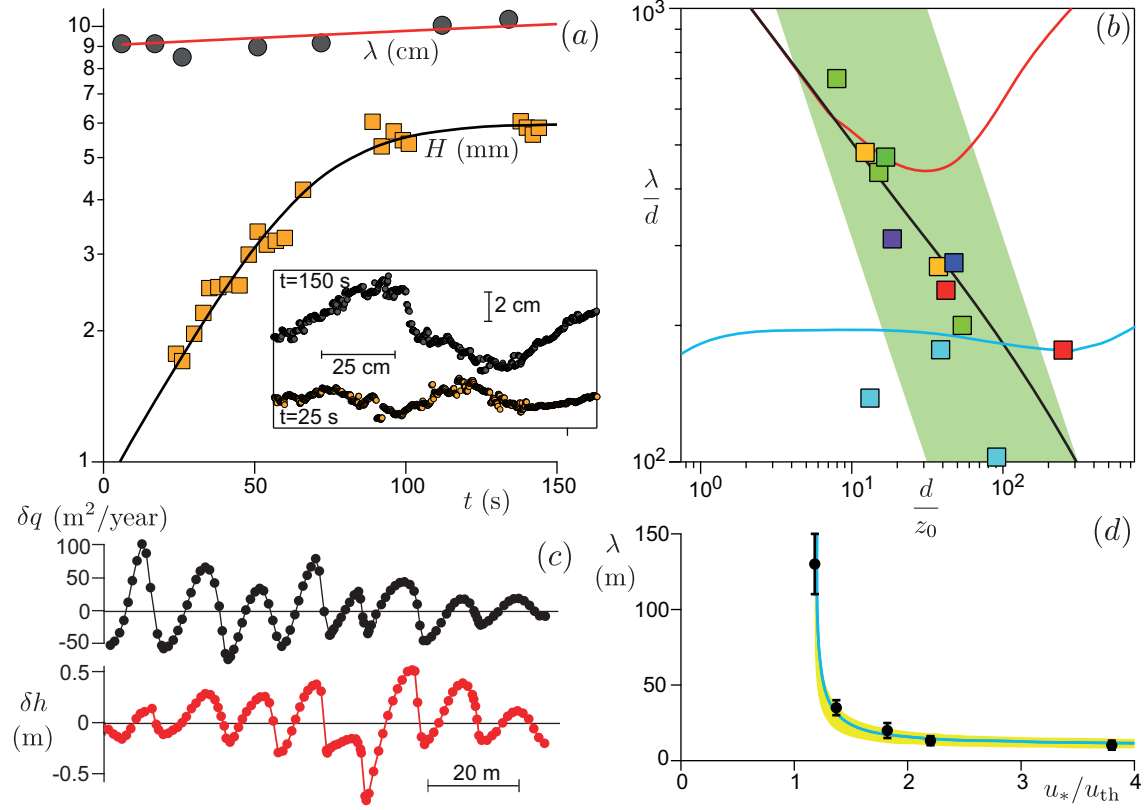


Figure 6: (a) Time evolution of the amplitude H (■) and wavelength λ (●) of ripples in a natural river in Gascogne, from a flat sand bed. Inset: bed profiles at $t = 25$ s and $t = 150$ s. (b) Measured initial wavelengths λ/d as a function of d/z_0 , for u_*/u_{th} in the range 1.8 ± 0.2 : ■, Coleman & Melville (1996); ■, Baas (1994, 1999); ■, Kuru et al. (1995); ■, Charru & Mouilleron (2002); ■, Langlois & Valance (2007); ■, Fourrière et al. (2010); ■, Betat et al. (1999). Solid lines: predictions for the most unstable wavelength, with $\mathcal{S} = 0.5$ and $L_{\text{sat}}/d = 2.5 U(d)/V_{\text{fall}}$ (rough case) and $L_{\text{sat}}/d = 12 U(d)/V_{\text{fall}}$ (smooth case), with color code as in Figure 3. (c) Profile δh of dunes on the flank of a large barchan and corresponding sand flux perturbation δq . (d) Measured initial wavelength of aeolian dunes as a function of the rescaled wind velocity. Yellow region: uncertainty on the value of L_{sat} , in the range 0.5–0.9 m.

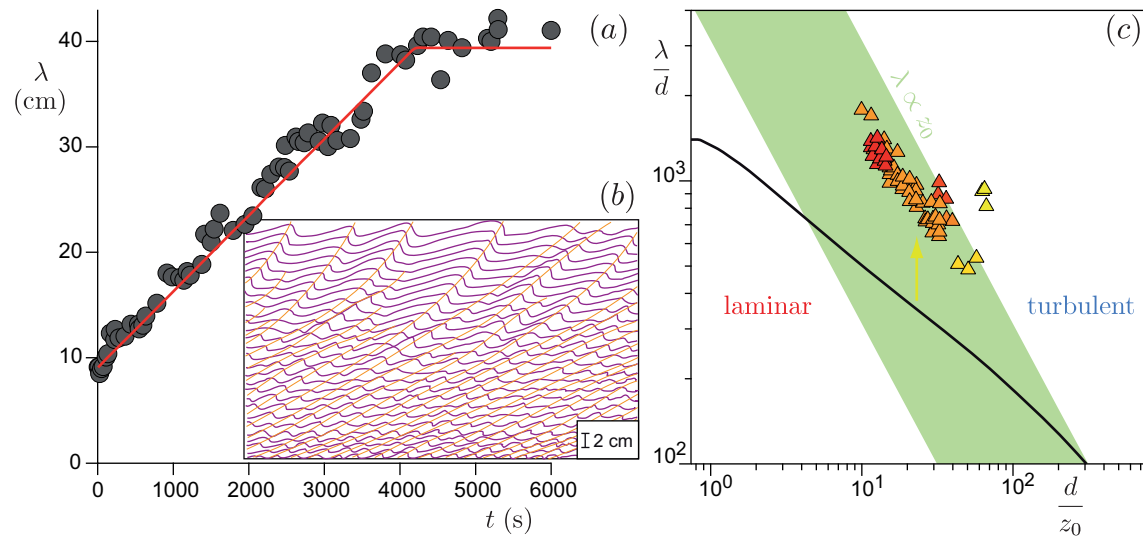


Figure 7: (a) Slow time evolution of the wavelength by pattern coarsening after the initial stage shown in Figure 6a, and saturation due to the influence of the river depth. (b) Spatiotemporal diagram of the nonlinear coarsening (Coleman & Melville 1994). (c) Wavelengths collected by Yalin (1985) for final subaqueous ripples (triangles), for $u_*/u_{th} < 1.5$, in the graph λ/d vs d/z_0 . The black line of Figure 6b (Hanratty's model) is reported for reference.

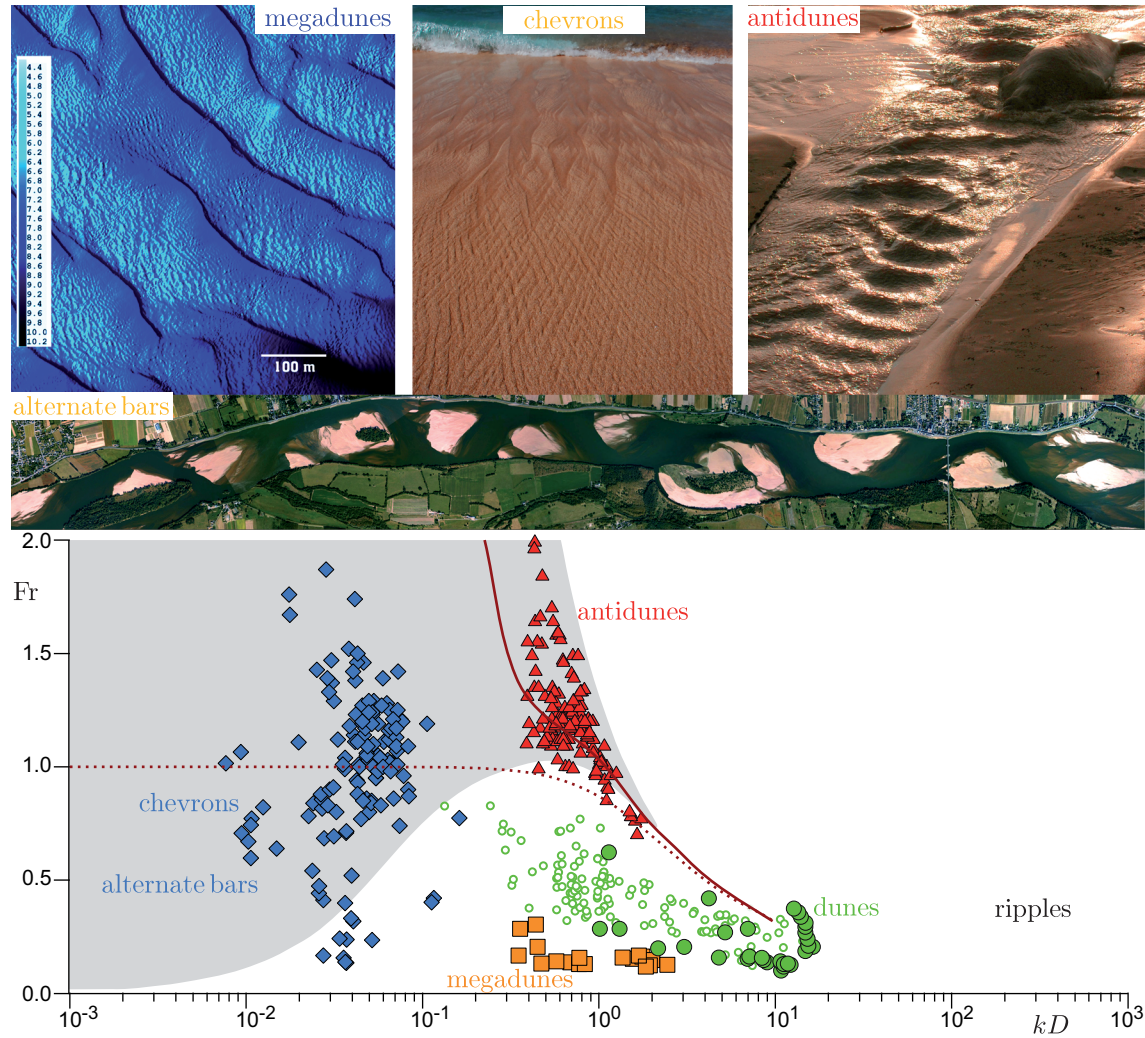


Figure 8: Top: photographs of bedforms with $kD \lesssim 1$ (finite-depth or finite-width effects). Bottom: data-set of natural bedforms in the plane (kD, Fr) ; green circles: dunes in flumes; grey region: $\mathcal{B} < 0$, white region: $\mathcal{B} > 0$.

References

1. Abrams, J. & Hanratty, T. J. 1985 Relaxation effects observed for turbulent flow over a wavy surface. *J. Fluid Mech.* **151**, 443–455.
2. Anderson, R. S., Haff, P. K., 1988. Simulation of aeolian saltation. *Science* **241**, 820–823.
3. Andreotti, B. 2004 A two species model of aeolian sand transport. *J. Fluid Mech.* **510**, 47–50.
4. Andreotti, B., Claudin, P. & Douady, S. 2002 Selection of dune shapes and velocities. Part 2: A two-dimensional modelling. *Eur. Phys. J. B* **28**, 341–352.
5. Andreotti, B., Claudin, P., Devauchelle, O. Durán, O. & Fourrière, A. 2012 Bedforms in a turbulent stream: ripples, chevrons and antidunes. *J. Fluid Mech.* **690** 94–128.
6. Andreotti, B., Claudin, P. & Pouliquen, O. 2010 Measurements of the aeolian sand transport saturation length. *Geomorphology* **123**, 343–348.
7. Andreotti, B., Fourrière, A., Ould-Kaddour, F., Murray, A.B., Claudin, P., 2009. Giant aeolian dune size determined by the averaged depth of the atmospheric boundary layer. *Nature* **457**, 1120–1123.
8. Ashida, K. & Okabe, T. 1982 On the calculation method of the concentration of suspended sediment under non-equilibrium condition. *Proc. 26th conf. hydraulics*, JSCE (in japanese), 153–158.
9. Ayotte, K. W., Xu, D. & Taylor, P. A. 1994 The impact of turbulence closure schemes on predictions of the mixed spectral finite-difference model for flow over topography. *Boundary-Layer Met.* **68**, 1–33.

10. Baas, J. H. 1994 A flume study on the development and equilibrium morphology of current ripples in very fine sand. *Sedimentology* **41**, 185–209.
11. Baas, J. H. 1999 An empirical model for the development and the equilibrium morphology of current ripples in fine sand. *Sedimentology* **46**, 123–138.
12. Baddock, M. C., Livingstone, I. & Wiggs, G. F. S. 2007 The geomorphological significance of airflow patterns in transverse dune interdunes, *Geomorphology* **87**, 322–336.
13. Bagnold, R. A. 1941 *The physics of blown sand and desert dunes*. Methuen, London.
14. Bagnold, R. A. 1956 The flow of cohesionless grains in fluids. *Phi. Trans. R. Soc. London A* **249**, 235–297.
15. Belcher, S. E. & Hunt, J. C. R. 1998 Turbulent flow over hills and waves. *Ann. Rev. Fluid Mech.* **30**, 507–538.
16. Benjamin, T. B. 1959 Shearing flow over a wavy boundary. *J. Fluid Mech.* **6**, 161–205.
17. Best, J. 2005 The fluid dynamics of river dunes: a review and some future research directions. *J. Geophys. Res.* **110**, F04S02.
18. Betat, A., Frette, V. & Rehberg, I. 1999 Sand ripples induced by water shear flow in an annular channel. *Phys. Rev. Lett.* **83**, 88–91.
19. Betat, A., Krülle, C.A., Frette, V. & Rehberg, I. 2002 Long-time behavior of sand ripples induced by water shear flow. *Eur. Phys. J. E* **8**, 465–476.
20. Blondeaux, P. 2001 Sand ripples under sea waves. Part 1. Ripple formation *J. Fluid Mech.* **218**, 1–17.

21. Blondeaux, P. 2001 Mechanics of coastal forms. *Annu. Rev. Fluid Mech.* **33**, 339–370.
22. Bordner, G. L. 1978 Nonlinear analysis of laminar boundary layer flow over a periodic wavy surface. *Phys. Fluids* **21**, 1471–1464.
23. Bourke, M. C., Lancaster, N., Fenton, L. K., Parteli, E. J. R., Zimbelman, J. R. & Radebaugh, J. 2010 Extraterrestrial dunes: an introduction to the special issue on planetary dune systems. *Geomorphology* **121**, 1–14.
24. Buckles, J., Hanratty, T. J. & Adrian, R. J. 1984 Turbulent flow over large-amplitude wavy surfaces. *J. Fluid Mech.* **140**, 27–44.
25. Caponi, E. A., Fornberg, B., Kight, D. D., McLean, J. W., Saffman, P. G. & Yuen, H. C. 1982 Calculations of laminar viscous flow over a moving wavy surface. *J. Fluid Mech.* **124**, 247–262.
26. Chang, H. Y., Simons, D. B. & Woolhiser, D. A. 1971 Flume experiments on alternate bar formation. *J. Waterways Harbors Coastal Eng. Div.* **97**, 155–165.
27. Charru, F. 2006 Selection of the ripple length on a granular bed sheared by a liquid flow. *Phys. Fluids* **18**, 121508.
28. Charru, F. & Franklin, E. 2012 Subaqueous barchan dunes in turbulent shear flow. Part 2. Fluid flow. *J. Fluid Mech.*, **694**, 131–154.
29. Charru, F. & Hinch, E. J. 2000 ‘Phase diagram’ of interfacial instabilities in a two-layer Couette flow and mechanism for the long-wave instability. *J. Fluid Mech.*, **414**, 195–223.
30. Charru, F., Hinch, E.J. 2006 Ripple formation on a particle bed sheared by a viscous liquid. Part 1. Steady flow. *J. Fluid Mech.* **550**, 111–121.

31. Charru, F., Hinch, E. J. 2006 Ripple formation on a particle bed sheared by a viscous liquid. Part 2. Oscillating flow. *J. Fluid Mech.* **550**, 123–137.
32. Charru, F. & Mouilleron-Arnould, H. 2002 Instability of a bed of particles sheared by a viscous flow. *J. Fluid Mech.* **452**, 303–323.
33. Charru, F., Mouilleron, H. & Eiff, O. 2004 Erosion and deposition of particles on a bed sheared by a viscous flow. *J. Fluid Mech.* **519**, 55–80.
34. Cherukat, P., Na, Y., Hanratty, T. J. & McLaughlin, J. B. 1998 Direct numerical simulation of a fully developed turbulent flow over a wavy wall. *Theoret. Comput. Fluid Dynamics* **11**, 109–134.
35. Claudin, P. & Andreotti, B. 2006 A scaling law for aeolian dunes on Mars, Venus, Earth, and for sub-aqueous ripples. *Earth Pla. Sci. Lett.* **252**, 30–44.
36. Claudin, P., Charru, F. & Andreotti, B. 2011 Transport relaxation time and length scales in turbulent suspensions. *J. Fluid Mech.* **671**, 491–506.
37. Coleman, S. E. & Melville, B. W. 1994 Bed-form development. *J. Hydraul. Eng.* **120**, 544–560.
38. Coleman, S. E. & Melville, B. W. 1996 Initiation of bed forms on a flat sand bed. *J. Hydraul. Eng.* **122**, 301–310.
39. Colombini, M. 2004 Revisiting the linear theory of sand dune formation. *J. Fluid Mech.* **502**, 1–16.
40. Colombini, M. & Stocchino, A. 2008 Finite-amplitude river dunes. *J. Fluid Mech.* **611**, 283–306.
41. Creyssels, M., Dupont, P., Ould el Moctar, A., Valance, A., Cantat, I., Jenkins, J. T., Pasini, J. M. & Rasmussen, K. R. 2009 Saltating particles in a turbulent boundary layer: experiment and theory. *J. Fluid Mech.* **625**, 47–74.

42. Daerr, A., Lee, P. Lanuza, J. & Clément, E. 2003 Erosion patterns in a sediment layer. *Phys. Rev. E* **67**, 065201(R).
43. de Angelis, V., Lombardi, P. & Banerjee, S. 1997 Direct numerical simulation of turbulent flow over a wavy wall. *Phys. Fluids* **9**, 2429–2442.
44. Devauchelle, O., Malverti, L., Lajeunesse, E., Josserand, C., Lagrée, P.-Y., & Métivier, F. 2010 Rhomboid beach pattern: a laboratory investigation. *J. Geophys. Res.* **115**, F02017.
45. Dey, S. 2003 Threshold of sediment motion on combined transverse and longitudinal sloping beds. *J. Hydraul. Res.* **41**, 405–415.
46. Durán, O., Claudin, P. & Andreotti B. 2011 On aeolian transport: grain-scale interactions, dynamical mechanisms and scaling laws. Review Article. *Aeolian Research* **3**, 243–270.
47. Elbelrhiti, H., Claudin, C., Andreotti, B., 2005 Field evidence for surface wave induced instability of sand dunes. *Nature* **437**, 720–723.
48. Engelund, F. 1970 Instability of erodible beds. *J. Fluid Mech.* **42**, 225–244.
49. Engelund, F. & Fredsøe, J. 1982 Sediment ripples and dunes. *Ann. Rev. Fluid Mech.* **14**, 13–37.
50. Fernandez Luque, R. & van Beek, R. 1976 Erosion and transport of bed-load sediment. *J. Hydraul. Res.* **14**, 127–144.
51. Finnigan, J. J., Raupach, M. R., Bradley, E. F. & Aldis G. K. 1990 A wind tunnel study of turbulent flow over a two-dimensional ridge. *Boundary-Layer Met.* **50**, 277–317.
52. Fourrière, A., Claudin, P. & Andreotti, B. 2010 Bedforms in a turbulent stream:

- formation of ripples by primary linear instability and of dunes by non-linear pattern coarsening. *J. Fluid Mech.* **649**, 287–328.
53. Frederick, K. A. & Hanratty, T. J. 1988 Velocity measurements for a turbulent nonseparated flow over solid waves. *Exp. Fluids* **6**, 477–486.
54. Fredsøe, J. 1974 On the development of dunes in erodible channels. *J. Fluid Mech.* **64**, 1–16.
55. Fryberger, S. G. & Dean, G. 1979 Dune forms and wind regime. In *A study of global sand seas*, E.D. McKee editor, Geological Survey Professional Paper 1052, Washington, 137–169.
56. Gong, W. & Ibbetson, A. 1989 A wind tunnel study of turbulent flow over model hills. *Boundary-Layer Met.* **49**, 113–148.
57. Gong, W., Taylor, P. A. & Dörnbrack, A. 1996 Turbulent boundary-layer flow over fixed aerodynamically rough two-dimensional sinusoidal waves. *J. Fluid Mech.* **312**, 1–37.
58. Gradowczyk, M. H. 1968 Wave propagation and boundary instability in erodible-bed channels. *J. Fluid Mech.* **33**, 93–112.
59. Greeley, R. Marshall, J. R. & R.N. Leach, R. N. 1984 Microdunes and other aeolian bedforms on Venus: wind tunnel simulations. *Icarus* **60**, 152–160.
60. Guy, H., Simons, D. & Richardson, E. 1966 Summary of alluvial channel data from flume experiments, 1956-61. *U.S. Geol. Survey Prof. Paper* **462-I**, 1–96.
61. Henn, D. S. & Sykes, R. I. 1999 Large-eddy simulation of slow over wavy surfaces. *J. Fluid Mech.* **383**, 75–112.
62. Hersen, P., Douady, S. & Andreotti, B. 2002 Relevant lengthscale of barchan dunes. *Phys. Rev. Lett.* **89**, 264301.

63. Ho, T.D., Valance, A., Dupont, P. & Ould El Moctar, A. 2011 Scaling laws in aeolian sand transport. *Phys. Rev. Lett.* **106**, 094501.
64. Hudson, J. D., Dykhno, L. & Hanratty, T. J. 1996 Turbulence production in flow over a wavy wall. *Exp. Fluids* **20**, 257–265.
65. Hunt, J. C. R., Leibovich, S. & Richards, K. J. 1988 Turbulent shear flows over low hills. *Q. J. R. Meteorol. Soc.* **114**, 1435–1470.
66. Iversen, J. D. & Rasmussen, K. R., 1999 The effect of wind speed and bed slope on sand transport. *Sedimentology* **46**, 723–731.
67. Jackson, P. S. & Hunt, J. C. R. 1975 Turbulent wind flow over a low hill. *Q. J. R. Meteorol. Soc.* **101**, 929–955.
68. Jensen, N.-O. & Zeman O. 1985 in International workshop on the physics of blown sand, edited by O.E. Barndorff-Nielsen, K. Moller, K.R. Rasmussen, B.B. Willets (University of Aarhus), 351–368.
69. Jobson, A. E. & Sayre, W. W. (1970), Vertical transfer in open channel flow. *J. Hydr. Div., ASCE* **96**, 703–724.
70. Kamphuis, J. W. 1974 Determination of sand roughness for fixed beds. *J. Hydraul. Res.* **12**, 193–207.
71. Kennedy, J. F. 1963 The mechanics of dunes and antidunes in erodible bed channels. *J. Fluid Mech.* **16**, 521–544.
72. Kennedy, J. F. 1969 The formation of sediment ripples, dunes and antidunes. *Ann. Rev. Fluid Mech.* **1**, 147–168.
73. Kroy, K., Sauermann, G. & Herrmann, H. J. 2002 Minimal model for aeolian sand dunes. *Phys. Rev. E* **66**, 031302.

74. Kruse, N., Günther, Q. & Rudolf von Rohr, P. 2003 Dynamics of large-scale structures in turbulent flow over a wavy wall. *J. Fluid Mech.* **485**, 87–96.
75. Kuru, W. C., Leighton, D. T. & McCready, M. J. 1995 Formation of waves on a horizontal erodible bed of particles. *Int. J. Multiphase Flow* **21**, 1123–1140.
76. Kuzan, J. D., Hanratty, T. J. & Adrian, R. J. 1989 Turbulent flows with incipient separation over solid waves. *Exp. Fluids* **7**, 88–98.
77. Lagrée, P.-Y. 2003 A triple deck model of ripple formation and evolution. *Phys. Fluids* **15**, 2355–2368.
78. Lajeunesse, E., Malverti, L. & Charru, F. 2010 Bedload transport in turbulent flow at the grain scale: experiments and modeling. *J. Geophys. Res.* **115**, F04001.
79. Langlois, V. & Valance, A. 2007 Formation and evolution of current ripples on a flat sand bed under turbulent water flow. *Eur. Phys. J. E* **22**, 201–208.
80. Lanzoni, S. 2000 Experiments on bar formation in a straight flume. 2. Uniform sediment. *Water Resources Res.* **36**, 3351–3363.
81. Leighton, D. & Acrivos, A. 1986 Viscous resuspension. *Chem. Engng Sci.* **41**, 1377–1384.
82. Lisle, T. E., Ikeda, H. & Iseya, F. 1991 Formation of stationary alternate bars in a steep channel with mixed-size sediment: a flume experiment. *Earth Surf. Proc. Landforms* **16**, 463–469.
83. Loiseleux, T., Gondret, P., Rabaud, M. & Doppler, D. 2005 Onset of erosion and avalanche for an inclined granular bed sheared by a continuous laminar flow. *Phys. Fluids* **17**, 103304.

84. Luchini, P. & Charru, F. 2010 The phase lead of shear stress in shallow-water flow over a perturbed bottom. *J. Fluid Mech.* **665**, 516–539.
85. Mason, P. J. & King, J. C. 1985 Measurements and predictions of flow and turbulence over an isolated hill of moderate slope. *Quart. J. R. Met. Soc.* **111**, 617–640.
86. McLean, S. R. 1990 The stability of ripples and dunes. *Earth-Science Rev.* **29**, 131–144.
87. Morton, R. A. 1978 Large-scale rhomboid bed forms and sedimentary structures associated with hurricane washover. *Sedimentology* **25**, 183–204.
88. Mouilleron, H., Charru, F. & Eiff, O. 2009 Inside the moving layer of a sheared granular bed. *J. Fluid Mech.* **628**, 229–239.
89. Narteau, C., Zhang, D., Rozier, O. & Claudin, P. 2009 Setting the length and time scales of a cellular automaton dune model from the analysis of superimposed bedforms. *J. Geophys. Res.* **114**, F03006.
90. Ouriemi, M., Aussillous, P. & Guazzelli, E. 2009 Sediment dynamics. Part 1. Bed-load transport by laminar shearing flows. *J. Fluid Mech.* **636**, 321–336.
91. Owen, P. R. 1964 Saltation of uniform grains in air. *J. Fluid Mech.* **20**, 225–242.
92. Parker, G. 1975 Sediment inertia as cause of river anti-dunes. *J. Hydr. Div., ASCE* **101**, 211–221.
93. Parteli, E. J. R., Schwämmle, V., Herrmann, H. J., Monteiro, L. H. U. & Maia L. P. 2006 Profile measurement and simulation of a transverse dune field in the Lençóis Maranhenses, *Geomorphology* **81**, 29–42.
94. Poggi, D., Katul, G. G., Albertson, J. D. & Ridolfi, L. 2007 An experimental investigation of turbulent flows over a hilly surface. *Phys. Fluids* **19**, 036601.

95. Pope, S. B. 2000. *Turbulent flows*. Cambridge University Press.
96. Pye, K. & Tsoar, H., 1990. *Aeolian sand and sand dunes*. Unwin Hyman, London.
97. Raudkivi, A. J. 2006 Transition from ripples to dunes. *J. Hydraul. Eng.* **132**, 1316–1320.
98. Raudkivi, A. J. & Witte, H. H. 1990 Development of bed features. *J. Hydraul. Eng.* **116**, 1063–1079.
99. Raupach, M. R., Antonia, R. A. & Rajagopalan, S. 1991 Rough-wall turbulent boundary layers. *Appl. Mech. Rev.* **44**, 1–25.
100. Richards, K. J. 1980 The formation of ripples and dunes on an erodible bed. *J. Fluid Mech.* **99**, 597–618.
101. Richards, K. J. & Taylor, P. A. 1981 A numerical model of flow over sand waves in water of finite depth. *Geophys. J. R. Astr. Soc.* **65**, 103–128.
102. Ross, A. N., Arnold, S., Vosper, S. B., Mobbs, S. D., Dixon, N. & Robins, A. G. 2004 A comparison of wind-tunnel experiments and numerical simulations of neutral and stratified flow over a hill. *Boundary-Layer Meteor.* **113**, 427–459.
103. Rousseaux, G., Stegner, A. & Wesfreid, J. E. 2004 Wavelength selection of rolling-grain ripples in the laboratory. *Phys. Rev. E* **69**, 031307.
104. Salvetti, M. V., Damiani, R. & Beux, F. 2001 Three-dimensional coarse large-eddy simulations of the flow above two-dimensional sinusoidal waves. *Int. J. Numer. Meth. Fluids* **35**, 617–642.
105. Sauermann, G., Kroy, K. & Herrmann, H. J. 2001 Continuum saltation model for sand dunes. *Phys. Rev. E* **64**, 031305.
106. Schaffinger, U., Acrivos, A. & Stibi, H. 1995 An experimental study of viscous

- resuspension in a pressure-driven plane channel flow. *Intl J. Multiphase Flow* **21**, 693–704.
107. Seminara, G. 2010 Fluvial Sedimentary Patterns, *Annu. Rev. Fluid Mech.* **42**, 43–66.
108. Silvestro, S., Fenton, L. K., Vaz, D. A., Bridges, N. T. & Ori, G. G. 2010 Ripple migration and dune activity on Mars: evidence for dynamic wind processes. *Geophys. Res. Lett.* **37**, L20203.
109. Sleath, J. F. A. 1976 On rolling-grain ripples. *J. Hydraul. Res.* **14**, 69–81.
110. Southard, J.B. 1991 Experimental determination of bed-form stability. *Ann. Rev. Earth Planet. Sci.* **19**, 423–455.
111. Stevenson, P., Thorpe, R. B., Kennedy, J. E. & McDermott, C. 2001 The transport of particles at low loading in near-horizontal pipes by intermittent flow. *Chem. Engng Sci.* **56**, 2149–2159.
112. Sumer, B.M. & Bakioglu, M. 1984 On the formation of ripples on an erodible bed. *J. Fluid Mech.* **144**, 177–190.
113. Sykes, R.I. 1980 An asymptotic theory of incompressible turbulent boundary-layer flow over a small bump. *J. Fluid Mech.* **101**, 647–670.
114. Taylor, P.A., Mason, P.J. & Bradley, E.F. 1987 Boundary-layer flow over low hills. *Boundary-Layer Met.* **39**, 107–132.
115. Ungar, J. E. & Haff, P. K. 1987 Steady state saltation in air. *Sedimentology* **34**, 289–299.
116. Valance, A. 2011 Nonlinear sand bedform dynamics in a viscous flow. *Phys. Rev. E* **83**, 036304.

117. Valance, A. & Langlois, V. 2005 Ripple formation over a sand bed submitted to a laminar shear flow. *Eur. Phys. J. B* **43**, 283–294.
118. van Boxel, J.H., Arens, A.M. & van Dijk, P.M. 1999 Aeolian processes across transverse dunes. I: Modelling the air flow. *Earth Surf. Processes Landforms* **24**, 255–270.
119. van Rijn, L.C. 1982 Equivalent roughness of alluvial bed. *J. Hydraul. Eng.* **108**, 1215–1218.
120. van Rijn, L.C. 1986 Application of sediment pickup function. *J. Hydraul. Eng.* **112**, 867–874.
121. Venditti, J. G., Church, M. A. & Bennett, S. J. 2005 Bed form initiation from a flat sand bed. *J. Geophys. Res.* **110**, F01009.
122. Walker, I. J. & Nickling, W. G. 2003 Simulation and measurement of surface shear stress over isolated and closely spaced transverse dunes in a wind tunnel. *Earth Surf. Processes Landforms* **28**, 1111–1124.
123. Weng, W. S., Hunt, J. C. R., Carruthers, D. J., Warren, A., Wiggs, G. F. S., Livingstone, I. & Castro, I. 1991 Air flow and sand transport over sand dunes. *Acta Mechanica* **2**, 1–22.
124. Wiggs, G. F. S., Livingstone, I. & Warren, A. 1996 The role of streamline curvature in sand dune dynamics: evidence from field and wind tunnel measurements. *Geomorphology* **17**, 29–46.
125. Yalin, M. S., 1985 On the determination of ripple geometry. *J. Hydraul. Eng.* **111**, 1148–1155.
126. Yue, W., Lin, C.-L. & Patel, V. C., 2006 Large-eddy simulation of turbulent flow over a fixed two-dimensional dune. *J. Hydraul. Eng.* **132**, 643–651.

127. Zilker, D. P., Cook, G. W. & Hanratty, T. J. 1977 Influence of the amplitude of a solid wavy wall on a turbulent flow. Part 1. Non-separated flows. *J. Fluid Mech.* **82**, 29–51.
128. Zilker, D. P. & Hanratty, T. J. 1979 Influence of the amplitude of a solid wavy wall on a turbulent flow. Part 2. Separated flows. *J. Fluid Mech.* **90**, 257–271.